(Supporting information)

Iodine Sequestration from Solution and Vapor Phase Systems Using Zr-Based Inorganic and Hybrid Polymeric Granules

*Meet Patel and Kalpana Maheria**

Department of Chemistry, Sardar Vallabhbhai National Institute of Technology, Ichchhanath, Surat - 395 007, Gujarat, India

*Corresponding Author's Email: kcm@chem.svnit.ac.in

Table of content

Section S1. Characterization techniques and instrumentation

S1.1: Powder X-ray diffraction (PXRD) data were recorded at room temperature using a PAnalytics X'Pert Pro diffractometer equipped with a microfocus rotating anode X-ray generator (Cu K_α radiation, λ=1.5418 Å) with a Ni filter. Data of ZrT and ZrT@PVDF composite were collected over the 2θ range of 5° to 80° with a scan rate of 1° min^{-1} and step size of 0.02°.

S1.2: Fourier transform infrared (FT-IR) spectroscopy was performed using a Shimadzu spectrophotometer in KBr pellet mode, covering a spectral range of 4000 to 400 cm^{-1} with a resolution of 4 cm^{-1}. Each sample was subjected to an average of 64 scans collection, with each sample analyzed twice.

S1.3: Thermogravimetric analysis (TGA) was performed before and after iodine adsorption using a TA Instruments Q600 thermogravimetric analyzer. Approximately 8-10 mg samples were placed in an alumina crucible and heated from 30 °C to 800 °C at a ramp rate of 10 °C/min under a nitrogen atmosphere.

S1.4: Field-emission scanning electron microscopy (FE-SEM) was performed using an FE-SEM Supra55 at a chamber pressure of 100/120 Pa to investigate the morphology and size of the materials. The analysis was conducted at an operating voltage of 10 and 15 kV and an electron beam current density of 150 pA, with a focal distance of 8 mm.

S1.5: The energy-dispersive X-ray spectroscopy (EDS) coupled with SEM was utilized to visualize the surface of the samples. The analysis was performed using a Bruker Quantax 200 system with a Z10 EDS detector.

S1.7: X-ray photoelectron spectroscopy (XPS) was performed on the adsorbent before and after iodine adsorption using a Thermo Scientific ESCALAB Xi+ system. Samples were mounted on carbon tape adhered to an aluminum stub. Photoelectron spectra were collected on an ESCALAB Xi+ XPS instrument equipped with Al Kα radiation, with a surface survey conducted using a 120 µm beam raster and a pass energy of 187.850 eV. High-resolution spectra of individual elemental regions were recorded at a pass energy of 29.350 eV. The spectra were calibrated by aligning the C 1s peak to 285 eV and fitted using iterated Shirley backgrounds followed by symmetric peak fitting.

S1.8: Inductively Coupled Plasma Optical Emission Spectroscopy (ICP-OES) was employed to determine metal concentrations using a PerkinElmer AVIO-200 instrument equipped with an AS93 autosampler.

S1.9: Raman Spectra before and after adsorption were collected using a Horiba Xplore Raman microscope equipped with a thermoelectrically cooled CCD detector and 785 nm laser

excitation source. Raman spectra for ZrT and ZrT@PVDF were obtained by accumulating three 10 s exposures over a spectral range of 100−3200 cm^{-1}, using 0.5% of the 300-mW laser power. For the iodine-loaded samples, the acquisition parameters were adjusted to static scans centered at 413 cm^{-1}, with 3−5 s exposures and 0.05% of the total laser power.

S2.0: Diffuse Reflectance UV-vis spectroscopy (UV-vis DRS) UV−vis spectroscopy measurements were conducted using a PerkinElmer Lambda 1050 spectrometer equipped with a photomultiplier R6872 detector for powder sample characterization. Spectra were recorded over the 200−850 nm range with a resolution of 1 nm. Diffuse reflectance spectra were analyzed using the Kubelka−Munk function.

S2.1: N_2 Isotherm Analysis The Brunauer-Emmett-Teller (BET) surface areas and pore structures of samples were measured on Nova Touch LX2 (Quantachrome Instruments) at 77 K. All samples were degassed at 100 °C for 24 h under vacuum before analysis. the BET equation was applied to calculate the specific surface area (m^2/g) within a relative pressure range of 0.05–0.30. The BJH pore size distributions were determined from the adsorption branches of the N2 isotherms.

Section S2. Iodine adsorption studies in aqueous and organic phases

Before conducting adsorption tests, iodine solutions were prepared in both water and cyclohexane by dissolving the desired quantity of iodine in each solvent. The mixtures were stirred at 500 rpm for 20 min, followed by sonication for 30 min. The factors influencing the adsorption isotherms and kinetics of ZrT and ZrT@PVDF were investigated using various experiment conditions, such as the effect of adsorption time (0.5–90 min for ZrT and 0.5–150 min for ZrT@PVDF at an initial iodine concentration of 1000 mg/L), varying iodine concentrations (50–1400 mg/L), and adsorbent dosages (5–40 mg), effect of *p*H (3-11). Six iodine solutions of known concentrations were employed to construct a calibration curve for determining unknown iodine concentrations at varied time periods.

Section S3. General procedure for selective adsorption of iodine

The adsorption of iodine was investigated in the presence of competing anions such as Cl^-, Br^-, NO_3^-, SO_4^{2-}, CH_3COO^- and CO_3^{2-}, using a mixed equimolar solution (500 mg/L, 1:1) containing both the targeted iodine and the competing anion. A 10 mg of ZrT was added to a binary solution containing 10 mL of 500 mg/L of target iodine and 10 mL of 500 mg/L of single, double and triple competing ions containing solution. After stirring the mixture for 2 h, it was filtered, and the resulting filtrate was analyzed by UV-vis spectroscopy.

Section S4. Iodine vapor-phase adsorption experiment

Iodine uptake experiments were conducted using a gravimetric technique under ambient pressure conditions. Precisely weighed samples of ZrT and ZrT@PVDF (20 mg each) were transferred into pre-weighed open glass vials (2 mL). These smaller vials were subsequently placed inside larger sealed glass vials (25 mL) containing an excess of iodine (0.5 g) at the bottom. Care was taken to ensure no physical contact occurred between the adsorbents and iodine. The tightly sealed larger vials were heated at 75 °C in an oven. At predefined time intervals, the smaller vials (containing the adsorbents were removed, cooled to room temperature, and reweighed. After recording the weight, the smaller vials were returned to the larger sealed vials, and the vial-in-vial setup was maintained at 75 °C to allow adsorption to proceed until the adsorbent weights reached equilibrium. The iodine uptake capacities (Q_t) of ZrT and ZrT@PVDF were calculated using Equation 1.

$$Q_t = \left(\frac{m_t - m_o}{m_o}\right) \quad (1)$$

Where Q_t (mg/g) represents the iodine vapor adsorbed capacity, and m_t and m_o (mg) are the weight of the adsorbent sample after and before the iodine vapor adsorption experiments, respectively.

Section S5. Column adsorption experiment

For the column adsorption experiment, a dry glass column [50 cm (length) × 1 cm (internal diameter)] was filled with glass wool at the bottom. 100 mg of the adsorbent was now introduced into the column, packed with glass wool at the top, and washed thoroughly with the appropriate solvent to remove air bubbles from the column, and then the dilute solution (500 mg/L) of iodine was passed through the column with maintain the flow rate at 0.1 mL/min. The obtained eluents were then examined using UV-Vis spectroscopy.

Section S6. Band-gap evaluation

The apparent band gap energy (E_g) of the materials was calculated based on the data acquired from UV-vis DRS. The E_g was determined by plotting the Kubelka-Munk function, $[F(R)hv]^n$, versus the photon energy (hv), where h is Planck constant (4.14×10^{-15} eV•s), v is the photon frequency (Hz). The index n corresponds to the type of electronic transition observed in the material during the investigation, such as indirect allowed transition ($n = 1/2$), direct allowed transition ($n = 2$), indirect forbidden transition ($n = 3$), and direct forbidden transition ($n =$

2/3). $F(R)$ is calculated using equation 2.[1] Where reflectance ($\% R$) was obtained from UV-vis DRS.

$$F(R) = \frac{(1-R)^2}{R} \quad (2)$$

Section S7. Stability Test

The stability of ZrT and ZrT@PVDF granules under various conditions was evaluated by immersing them in 0.1 N NaOH, 0.1 N HCl, and 0.1 N NaCl solutions for 24 h. To further assess their stability in aqueous environments, the ZrT and ZrT@PVDF were stirred continuously in water for 48 h, followed by filtration. The resultant supernatants were analyzed by ICP-OES to quantify the residual concentration of zirconium ions in the water. Elemental analysis revealed no detectable traces of Zr in the filtrate, indicating that both ZrT and ZrT@PVDF remained stable under the tested immersion conditions.

Section S8. Recovery of solid iodine through thermal treatment

The recovery of solid iodine was conducted using a laboratory-designed setup, as illustrated in Fig. S15 A. A specified amount of iodine-loaded compound (ZrT-I_2), captured via an aqueous phase, was thermally treated in an enclosed chamber at approximately 130 °C. Upon heating, iodine vapor generated from the compound was collected in a separate glass apparatus, which was immersed in an ice bath to promote condensation over a designated duration. After removing the glass flask from the system, solid iodine crystals were observed on its surface. These crystals were subsequently quantified and transferred to a separate storage vial.

Section S9. Precipitation of solid iodine by treatment with methanol

A specific amount of iodine-loaded compound (ZrT-I_2), captured via an aqueous phase, was treated with an exceeded amount of methanol. Upon treatment, the methanol solution turned dark brown, indicating the release of a large amount of iodine from ZrT-I_2. The methanol solution containing iodine was subsequently transferred to a glass Petri dish and allowed to evaporate at ambient temperature over several minutes. Upon complete evaporation of methanol, a substantial amount of solid iodine was precipitated on the surface of the glass Petri dish (Fig. S17). The iodine crystals were collected and transferred to a separate glass vial for storage.

Table S1. Characteristic FT-IR absorption frequencies and vibration mode of PVDF[2]

Band position (cm^{-1})	Phase	Vibration mode
482	α	CF_2 and CCC in phase bending, CF_2 in phase wagging, and CF_2 out of phase rocking
530	α	CF_2 bending, CCC out-of-phase bending, and CF_2 in- phase rocking
608	α	CF_2 in phase bending and wagging
755	α	CF_2 out of phase wagging, CCC out of phase bending
795	α	CH_2 rocking
833	$\beta + \gamma$	CH_2 rocking, CF_2 antisymmetric stretching
871	$\alpha + \beta + \gamma$	CF_2 symmetric stretching, CH_2 in-phase twisting, CC out-of-phase symmetric stretching
980	α	CH_2 out of phase twisting, CF_2 in phase symmetric stretching
1070	$\alpha + \beta + \gamma$	CH_2 and CF_2 wagging, CC antisymmetric stretching, CF_2, and CC out-of-phase antisymmetric stretching
1174	$\alpha + \beta + \gamma$	CF_2 and CC out of phase symmetric stretching, CF_2 in phase and out of phase antisymmetric stretching, CF_2 out of phase bending
1234	γ	CF out of plane deformation
1277	β	CH_2 and CF_2 rocking and CF_2 antisymmetric stretching
1396	$\alpha + \beta + \gamma$	CH_2 wagging, and CC symmetric stretching

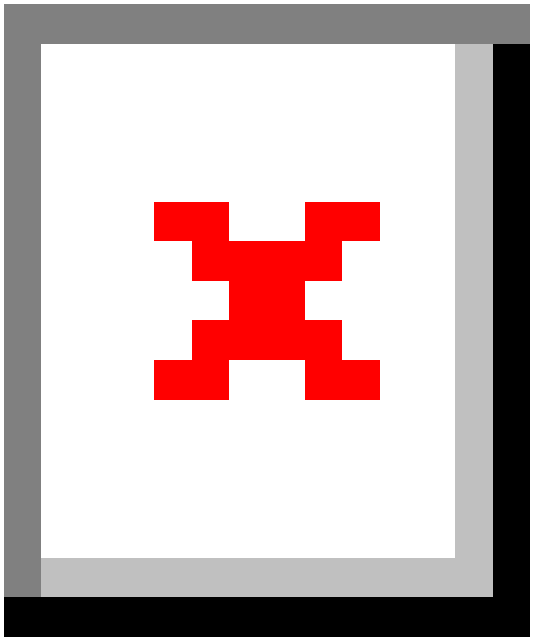

Figure S1. (A) 3D reconstruct FE-SEM image of ZrT (B) FE-SEM image of ZrT, and (C1-C4) FE-SEM mapping images of ZrT

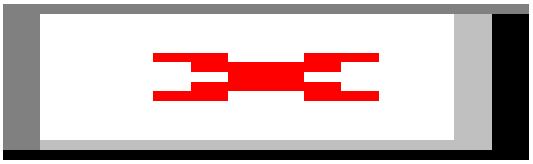

Figure S2. SEM-EDS spectrum of ZrT and ZrT@PVDF

Table S2. Removal efficiency of iodine in the aqueous and organic phase using ZrT@PVDF granules with varying ZrT doping concentrations

Sr. No.	granules	Wt.% of ZrT	% Removal efficiency		
			saturated I_2	I_3^- solution	I_2/cyclohexane
1	G_1	5	26.5	28.5	20.2
2	G_2	10	53.2	57.2	46.8
3	G_3	15	72.3	77.3	64.5
4	G_4	20	92.8	96.3	85.6

Experimental conditions: *Iodine concentration = 1000 mg/L; Adsorbent amount = 10 mg; Time = 3 h. ; Temp. = 30 °C*

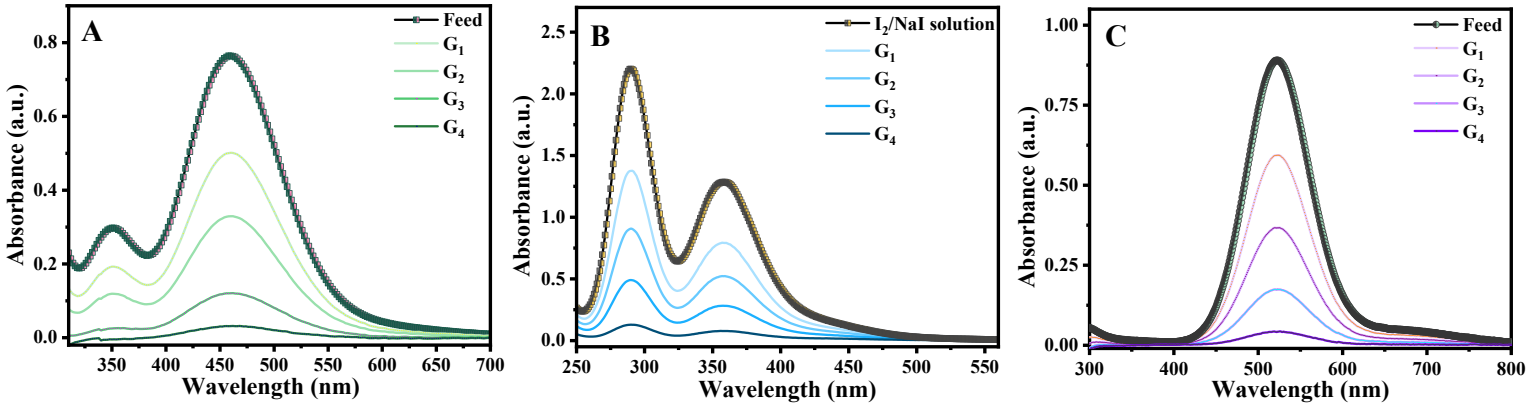

Figure S3. UV-vis spectrum of (A) saturated I_2, (B) I_3^- adsorption in the aqueous phase, and (C) iodine adsorption in organic phases using ZrT@PVDF granules with varying ZrT doping concentrations

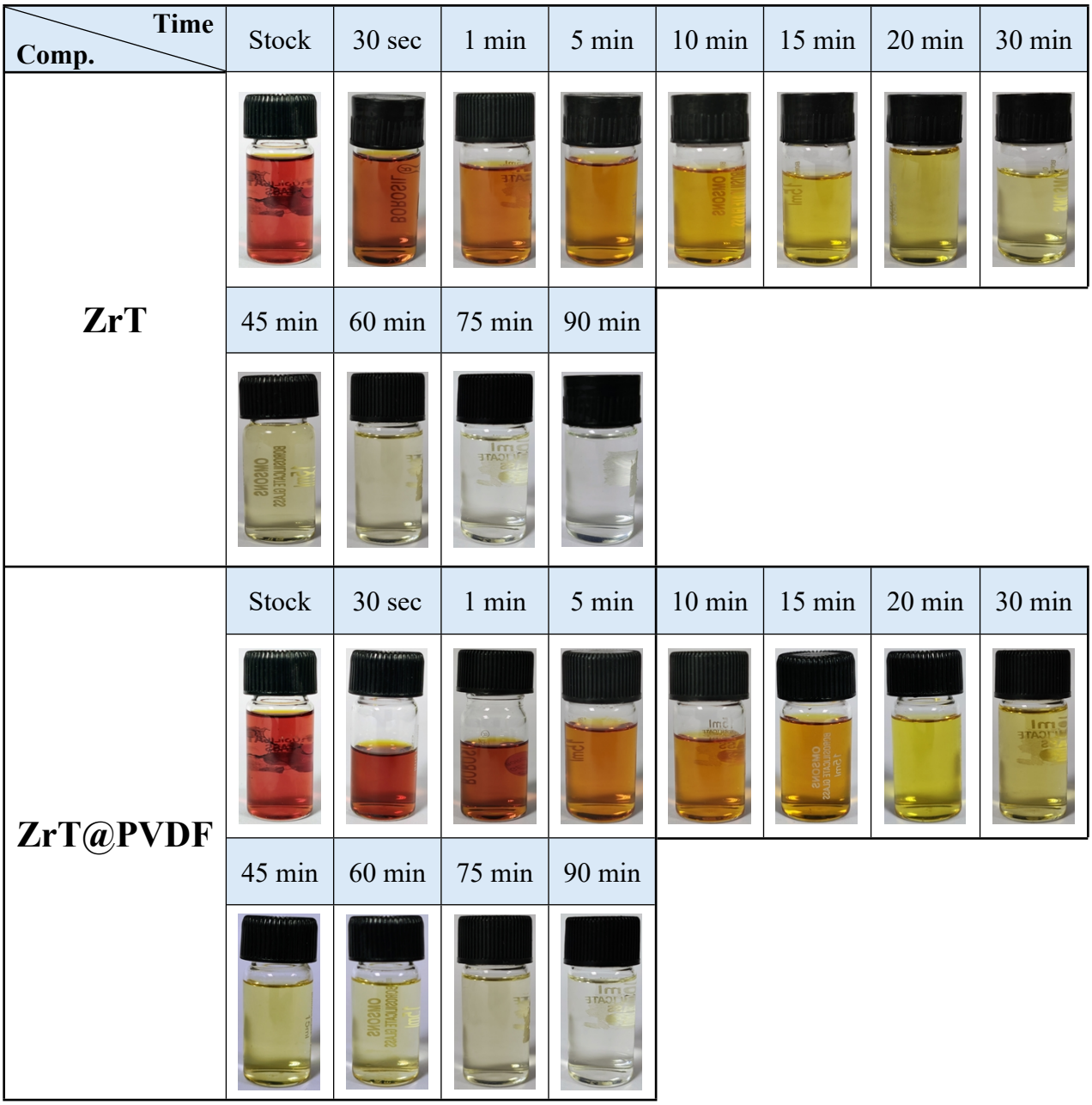

Figure S4. Digital images demonstrate the time-dependent color change in iodine-saturated aqueous solutions treated with ZrT and ZrT@PVDF

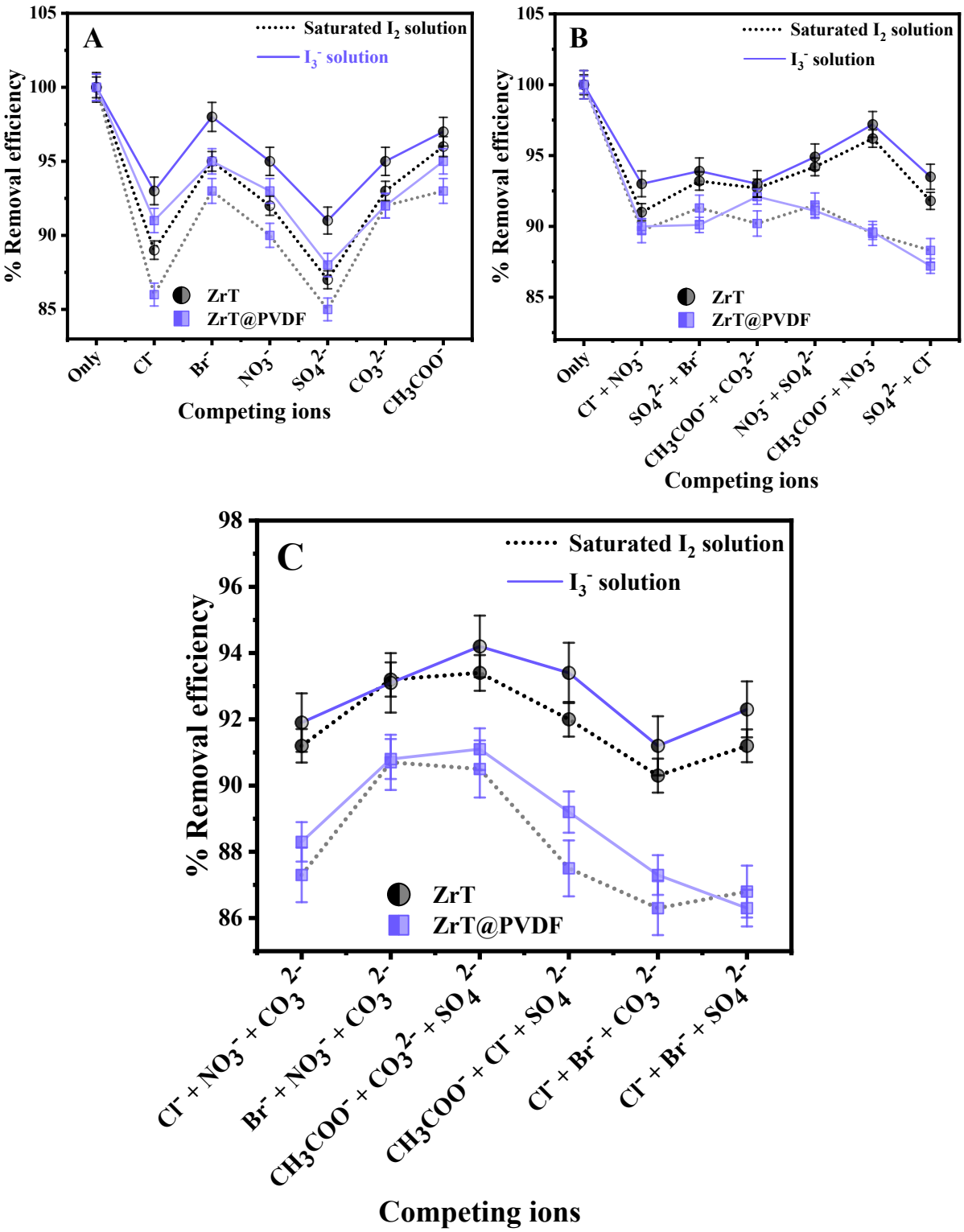

Figure S5. Selectivity of ZrT and ZrT@PVDF for iodine adsorption in the presence of (A) single, (B) double, and (C) Triple competing ions system

Figure S6. Digital images demonstrate the time-dependent color change in iodine-saturated cyclohexane solutions treated with ZrT and ZrT@PVDF

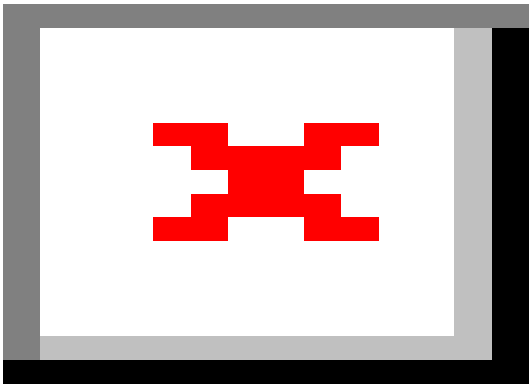

Figure S7. Photographs of the column packed with ZrT (A, E) and ZrT@PVDF (C, G) for iodine capture, UV-Vis spectra illustrate the saturated iodine in aqueous phase (B, D) and cyclohexane phase (F, H) before and after passing through the respective columns packed with ZrT and ZrT@PVDF

Section S10. Adsorption kinetics studies

Kinetic studies were carried out to elucidate the adsorption mechanism and rate of iodine uptake, with particular attention to diffusion processes and the influence of contact time between the liquid and solid phases.[3] During the adsorption process, solute exchange occurs between the liquid phase and solid surfaces through mass transfer mechanisms. To understand the kinetics of iodine adsorption onto ZrT and ZrT@PVDF composite, the experimental data collected at various contact times were fitted using pseudo-first-order (PFO) (equation 3) and pseudo-second-order (PSO) (equation 4) models.[4] It is noteworthy that the PFO model assumes the adsorption process is predominantly governed by the diffusion step. In contrast, the PSO model is based on the premise that chemical adsorption is the dominant factor influencing the adsorption rates.[5]

$$log(q_e - q_t) = logq_e - \frac{k_1}{2.303}t \quad (3)$$

$$\frac{t}{q_t} = \frac{1}{k_2 q_e^2} + \frac{1}{q_e}t \quad (4)$$

Here, k_1 (min^{-1}) and k_2 (g/mg min) represent the rate constants for the PFO and PSO, respectively. q_e and q_t denote the amount of iodine adsorbed (in mg/g) at equilibrium and at a specific time t, respectively.

The adsorption rate is typically governed by either an intraparticle or external diffusion process. The Weber-Morris intraparticle diffusion model (equation 5) has been employed to identify the rate-controlling step in the iodine adsorption process.[6]

$$q_t = k_{id} t^{0.5} + l \quad (5)$$

Where k_{id} represents the intra-particle diffusion coefficient (mg/g $min^{0.5}$), and l is associated with the thickness of the boundary layer.

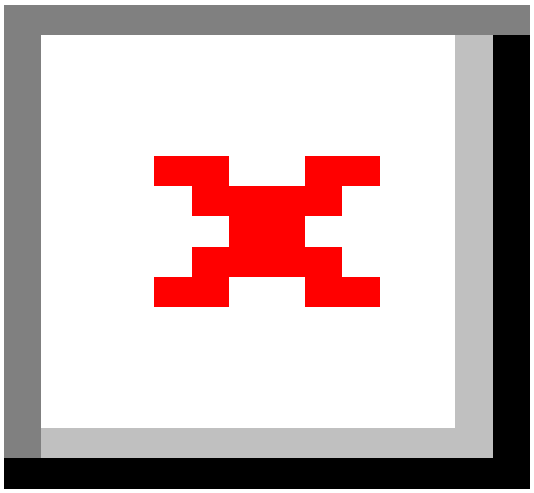

Figure S8. Pseudo-first-order (A, B) and pseudo-second-order (C, D) linear fitting curves for iodine adsorption onto ZrT and ZrT@PVDF. (A, C) represent the adsorption in the aqueous phase, while (B, D) represent the adsorption in the organic phase

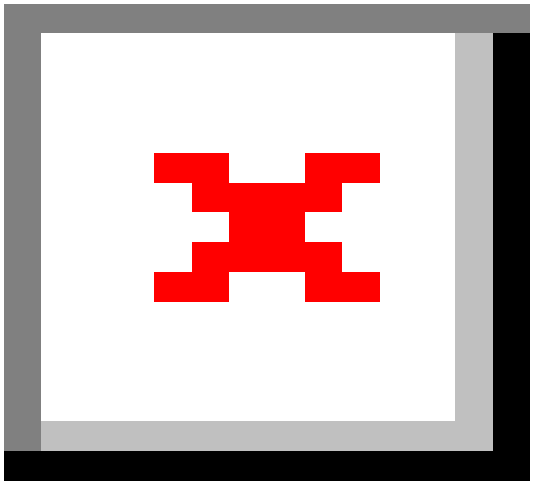

Figure S9. Pseudo-first-order (A, B) and pseudo-second-order (C, D) kinetics plots for iodine adsorption onto ZrT and ZrT@PVDF. (A, C) represent the adsorption in the aqueous phase, while (B, D) represent the adsorption in the organic phase

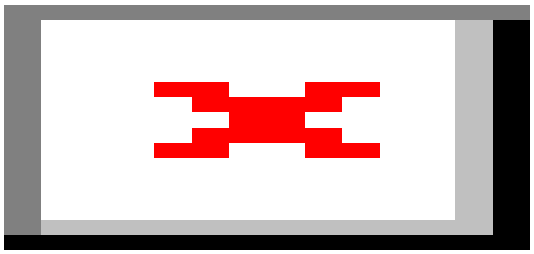

Figure S10. Intra-particle diffusion model for iodine adsorption onto ZrT and ZrT@PVDF in (A) aqueous phase and (B) organic phase

Table S3. Kinetics parameters for iodine adsorption in aqueous phase onto ZrT and ZrT@PVDF

I_2 in water	*Pseudo-First order*			*Pseudo-Second order*		
	k_1 (1/min)	*q_e (cal.)*	*R^2*	*K_2 (g/mg min)*	*q_e (cal.)*	*R^2*
ZrT	0.126	858	0.89	2.52×10^{-4}	886	0.99
ZrT@PVDF	0.157	653	0.79	3.11×10^{-4}	699	0.99
Weber-Morris model (intra-particle diffusion model)						
I_2 in water	*Initial phase*			*Secondary phase*		
	k_{id1}	*l_1*	*R^2_1*	*k_{id2}*	*l_2*	*R^2_2*
ZrT	141	112	0.97	15.41	747	0.98
ZrT@PVDF	100.9	121	0.86	13.64	577	0.93

Table S4. Kinetics parameters for iodine adsorption in organic phase onto ZrT and ZrT@PVDF

I_2 in cyclohexane	*Pseudo-First order*			*Pseudo-Second order*		
	k_1 (1/min)	*q_e (cal.)*	*R^2*	*K_2 (g/mg min)*	*q_e (cal.)*	*R^2*
ZrT	0.11	735	0.93	2.35×10^{-4}	764	0.99
ZrT@PVDF	0.055	577	0.95	1.4×10^{-4}	604	0.99
Weber-Morris model (intra-particle diffusion model)						
I_2 in cyclohexane	*Initial phase*			*Secondary phase*		
	k_{id1}	*l_1*	*R^2_1*	*k_{id2}*	*l_2*	*R^2_2*
ZrT	109.8	54	0.87	2.18	744	0.97
ZrT@PVDF	73.88	22	0.91	4.07	550	0.98

Section S11. Adsorption isotherm studies

The study of adsorption isotherms is crucial for understanding the surface properties of adsorbents, the adsorption mechanisms, and the interactions between adsorbents and adsorbates.[7] To elucidate the equilibrium distribution of iodine between the solid and liquid phases, the sorption isotherms were analyzed by fitting the equilibrium experimental data to six different isotherm models (Table S5). These models include two-parameter isotherms-Langmuir, Freundlich, Temkin, and Dubinin-Radushkevich (D-R) as well as three-parameter isotherms, specifically Sips and Redlich-Peterson (R-P). [4] The Langmuir isotherm is commonly employed to characterize the adsorption isotherms of ions and molecules. It posits that the adsorption on the surface of the adsorbent occurs via a single mechanism, resulting in the formation of a monomolecular layer of the adsorbate. Furthermore, it assumes that all active

sites on the adsorbent exhibit uniform energy and enthalpy characteristics.[8] Additionally, the separation (or equilibrium) factor (R_L) emerges as another critical parameter, providing insight into the monolayer adsorption dynamics, which is also evaluated herein and determined by equation 6.[8]

$$R_L = \frac{1}{1 + K_L C_o} \tag{6}$$

The R_L value determines if the process is unfavorable ($R_L > 1$), linear ($R_L = 1$), favorable ($0 < R_L < 1$), or irreversible ($R_L = 0$).

The Freundlich isotherm is applied to describe adsorption on heterogeneous surfaces, where adsorption sites exhibit varying energy levels. In this model, the highest-energy sites are occupied first, followed progressively by those with lower energy.[4] The Temkin model suggests that adsorption energy decreases linearly with increasing surface coverage due to the interaction between the adsorbent and adsorbate. It assumes a uniform distribution of binding energies across the surface sites, which is influenced by the density and spatial arrangement of functional groups on the adsorbent surface.[8] The Sips isotherm combines features of the Langmuir and Freundlich models and assumes that each adsorption site on a heterogeneous surface can bind only one adsorbate molecule and that the total number of available sites is finite and fixed.[9] The R-P isotherm is a hybrid adsorption model that incorporates characteristics of both the Langmuir and Freundlich isotherms.[10]

To investigate the adsorption mechanisms, the equilibrium data were analyzed using the D-R isotherm model. The D-R isotherm offers a more generalized approach compared to the Langmuir isotherm, as it does not rely on the assumptions of surface homogeneity or constant adsorption potential.[8] This isotherm is commonly employed to elucidate the mechanism of adsorbate interaction with the adsorbent, distinguishing between physical and chemical adsorption, and calculate the mean free energy (equation 7) associated with the adsorption process (E kJ/mol). [11]

$$E = \frac{1}{\sqrt{2K_D}} \tag{7}$$

At E values below 8 kJ/mol, adsorption predominantly occurs through physical interactions. When E falls within the range of 8-16 kJ/mol, ion exchange becomes the primary mechanism, whereas chemisorption dominates at E values between 16 and 40 kJ/mol.[11]

Table S5. Isotherm models used for iodine adsorption in aqueous and organic phase

Isotherm type	Linear Forms of the Equations[a]	Non-linear forms of the Equations[a]	Isotherm parameters	Ref.
Langmuir	$\frac{1}{q_e} = \left(\frac{1}{K_L q_m}\right)\frac{1}{C_e} + \frac{1}{q_m}$	$q_e = \frac{q_m K_L C_e}{1 + K_L C_e}$	q_m, K_L	12
Freundlich	$\log q_e = \log K_f + \frac{1}{n}\log C_e$	$= K_f C_e^{\frac{1}{n}}$	K_f, n	13
Temkin	$q_e = b\ln K_T + b\ln C_e$	$q_e = \frac{RT}{b}\ln\left(K_T C_e\right)$	K_t, b	14
Sips	$\ln\left(\frac{q_e}{q_m - q_e}\right) = \frac{1}{n}\ln C_e + \ln\left(K_s\right)^{\frac{1}{n}}$	$q_e = \frac{q_m\left(K_s C_e\right)^{\frac{1}{n}}}{1 + \left(K_s C_e\right)^{\frac{1}{n}}}$	K_s	15
Redlich-Peterson	$\ln\left(K_{RP}\frac{C_e}{q_e} - 1\right) = \beta\ln C_e + \ln\alpha_{RP}$	$q_e = \frac{K_{RP} C_e}{1 + \alpha_{RP} C_e^{\beta}}$	K_{RP}, α_{RP}	16
Dubinin-Radushkevich	$\ln q_e = \ln q_m - \beta\varepsilon^2$	$q_e = q_m e^{-\beta\varepsilon^2}$	ε, β	17

[a]Where, q_e, amount of iodine adsorbed at equilibrium (mg/g); q_m, maximum adsorption capacity of adsorbent (mg/g); C_e, equilibrium Conc. of the iodine (mg/L); K_L, Langmuir isotherm constant (mg/g); K_f, Freundlich isotherm constant (mg/g); K_t, Temkin constant (L/mg); b, equilibrium binding (J/mg); K_S, Sips isotherm constant (mg/g); K_{RP}, Redlich-Peterson isotherm constant; n, exponent of the adsorption process; β, Dubinin-Radushkevich isotherm constant (mol^2/KJ^2); α, Redlich-Peterson isotherm constant (L/mg); ε, Polanyi potential.

The χ^2 test statistic is determined by summing the squared deviations between the observed and model-predicted data, with each term normalized, the corresponding model-predicted values, as described in equation 8.[18]

$$\chi^2 = \sum \frac{(q_e - q_{e,cal})^2}{q_{e,cal}} \tag{8}$$

A low χ^2 value signifies a strong correspondence between the model and experimental data, whereas a high χ^2 value indicates substantial deviation.

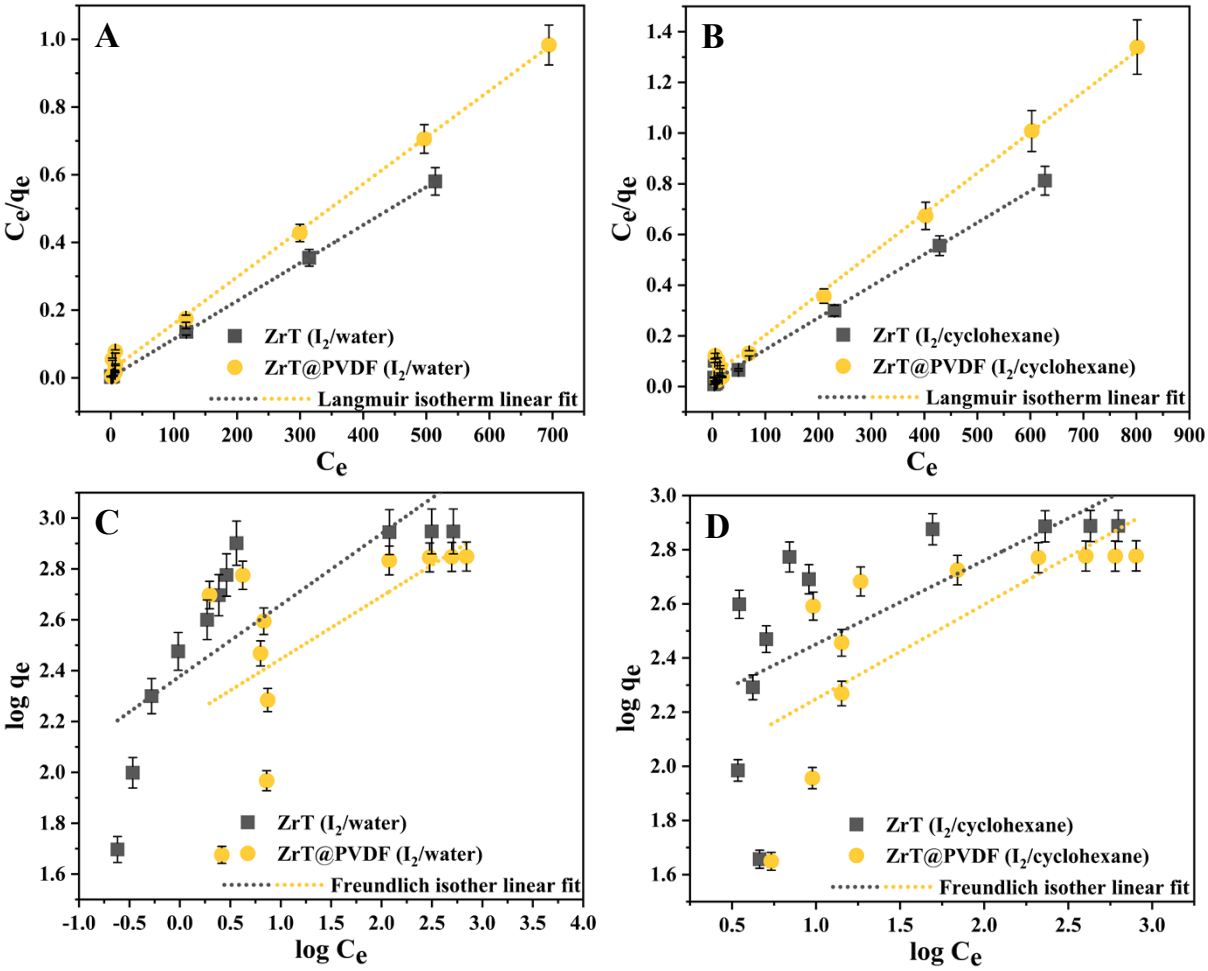

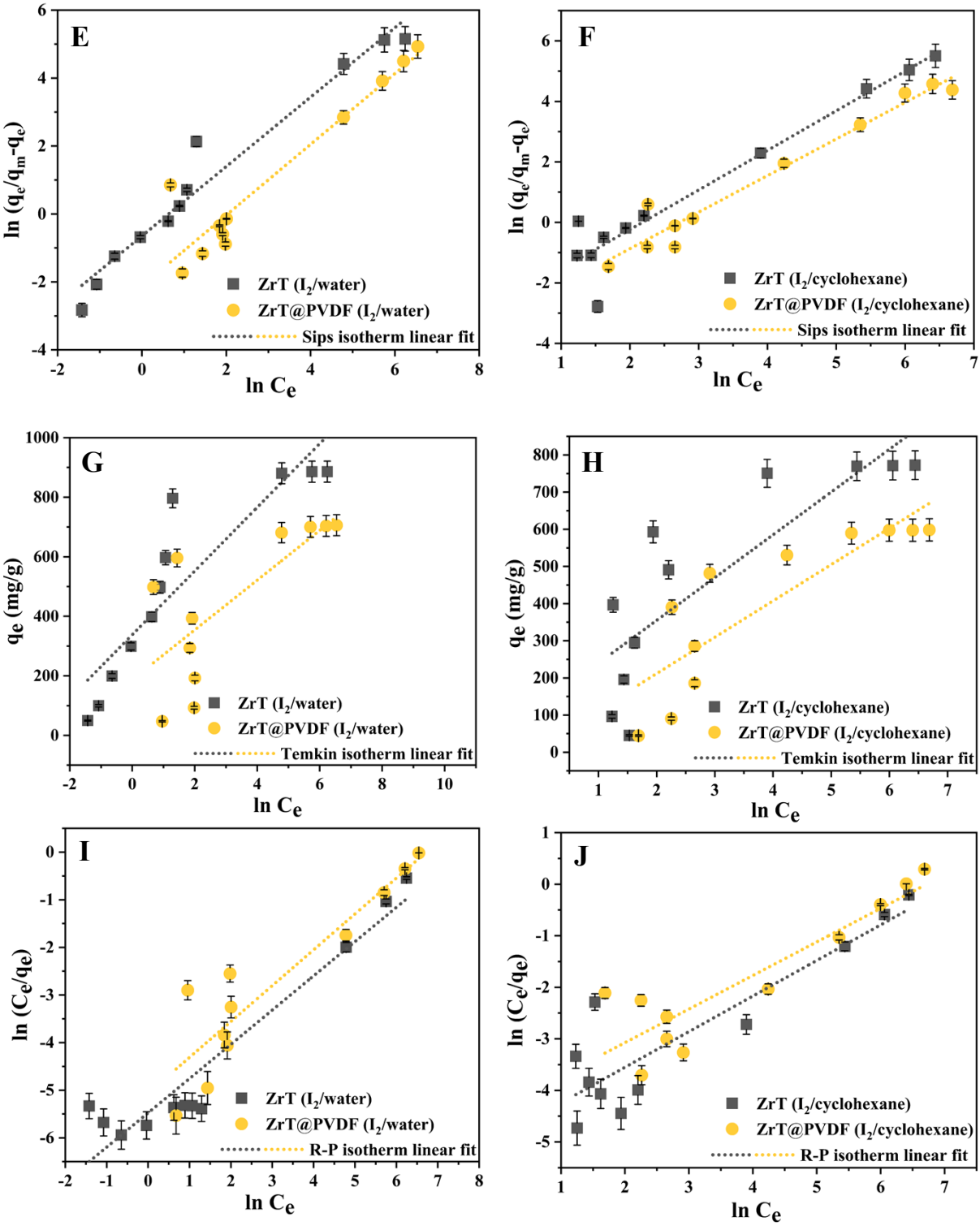
E
ln (qe/qm-qe)
ln Ce
ZrT (I2/water)
ZrT@PVDF (I2/water)
Sips isotherm linear fit
F
ln (qe/qm-qe)
ln Ce
ZrT (I2/cyclohexane)
ZrT@PVDF (I2/cyclohexane)
Sips isotherm linear fit
G
qe (mg/g)
ln Ce
ZrT (I2/water)
ZrT@PVDF (I2/water)
Temkin isotherm linear fit
H
qe (mg/g)
ln Ce
ZrT (I2/cyclohexane)
ZrT@PVDF (I2/cyclohexane)
Temkin isotherm linear fit
I
ln (Ce/qe)
ln Ce
ZrT (I2/water)
ZrT@PVDF (I2/water)
R-P isotherm linear fit
J
ln (Ce/qe)
ln Ce
ZrT (I2/cyclohexane)
ZrT@PVDF (I2/cyclohexane)
R-P isotherm linear fit

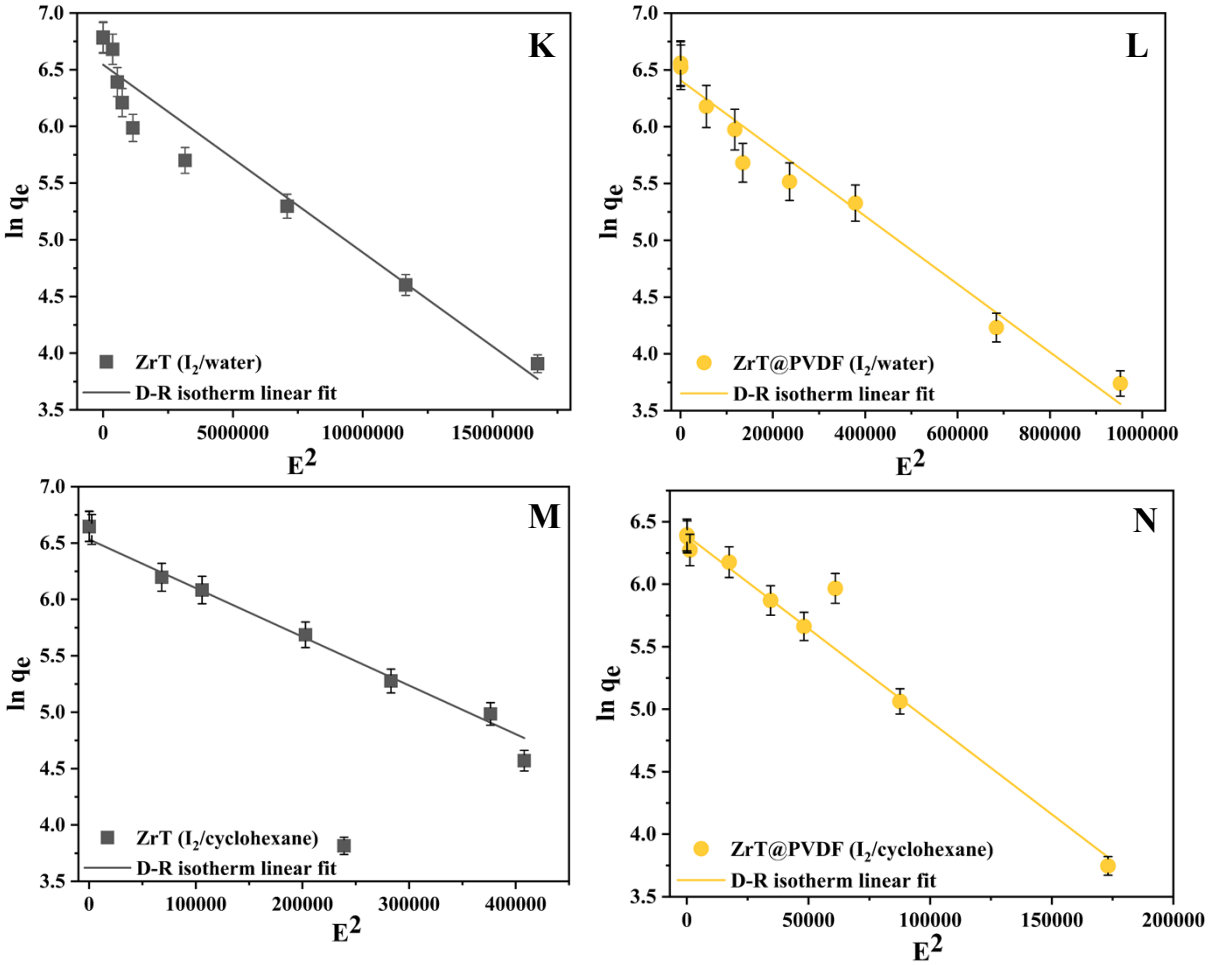

Figure S11. Linear isotherm models for iodine adsorption onto ZrT and ZrT@PVDF in the aqueous phase (A, C, E, G, I, K, L) and organic phase (B, D, F, H, J, M, N) fitted using six isotherm models

Table S6. Isotherm parameters for iodine adsorption in aqueous and organic phase onto ZrT and ZrT@PVDF

Isotherm type	*Isotherm Parameters*	*I_2/water*		*I_2/cyclohexane*	
		ZrT	*ZrT@PVDF*	*ZrT*	*ZrT@PVDF*
Langmuir	q_m *(mg/g)*	896	702	765	599
	k_L	0.74	0.14	0.12	0.068
	R_L	1.9×10^{-3}	2.3×10^{-3}	1.46×10^{-4}	1.3×10^{-4}
	χ^2	0.11	0.021	0.067	0.0017
	R^2	0.99	0.98	0.99	0.99
Freundlich	k_F	362	239	64	162
	n_F	6.18	5.64	5.016	4.71
	1/n	0.16	0.17	0.2	0.21
	R^2	0.71	0.54	0.44	0.54
Sips	q_m *(mg/g)*	900	720	780	590
	k_S	0.07	0.035	0.014	0.005
	n	0.97	0.95	1.05	1.1
	χ^2	0.24	0.30	0.075	0.11
	R^2	0.95	0.92	0.93	0.95
Temkin	K_T	23.6	9.43	2.95	1.18
	b	106.9	83.5	115	97.7
	R^2	0.82	0.53	0.70	0.73
Redlich-Peterson	k_{RP} *(L/g)*	376	55.7	81.3	31
	α (L/mg)	0.25	0.034	0.06	0.029
	β	0.09	0.52	0.092	0.38
	R^2	0.97	0.99	0.91	0.92
Dubinin-Radushkevich	k_D *(mol²/kJ²)*	2.96	7.51	27.51	119.1
	E (kJ/mol)	0.41	0.25	0.13	0.06
	R^2	0.94	0.97	0.96	0.95

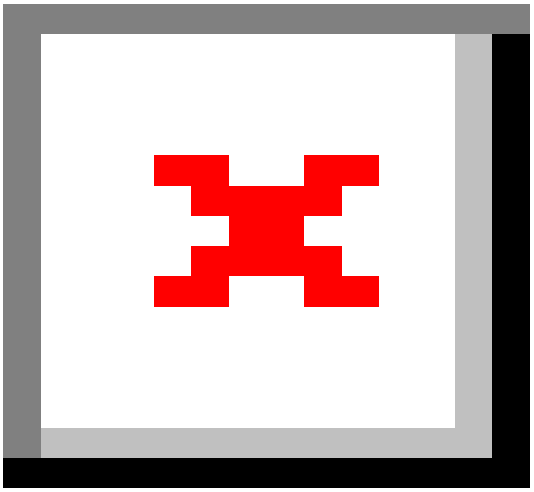

Figure S12. Non-linear isotherms models for iodine adsorption onto ZrT and ZrT@PVDF in aqueous (A, B) and organic (C, D) phases, fitted using six isotherm models

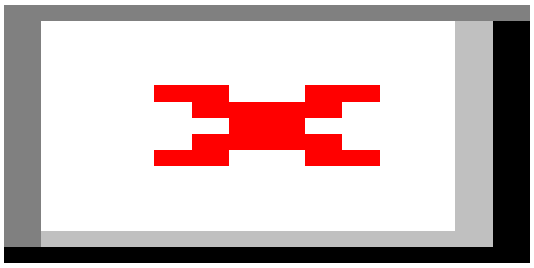

Figure S13. High-resolution spectra of O 1s for (A) ZrT and (B) ZrT@PVDF before and after iodine adsorption

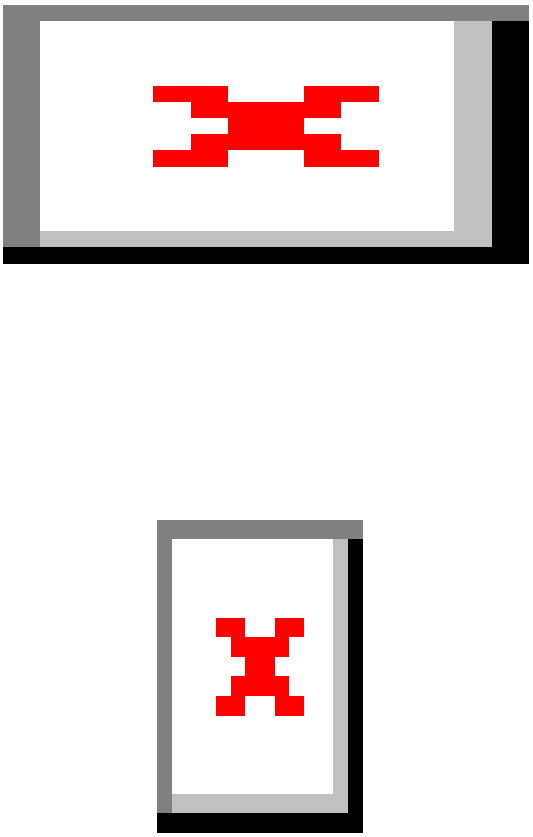

Figure S14. Schematic representation and a digital image of recovery of solid iodine setup by heating of ZrT-I_2 at ~130 °C

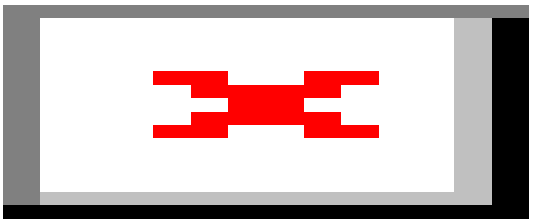

Figure S15. Digital image (A) shows images of the solid iodine recovery laboratory-designed setup and (B) recovered iodine crystals

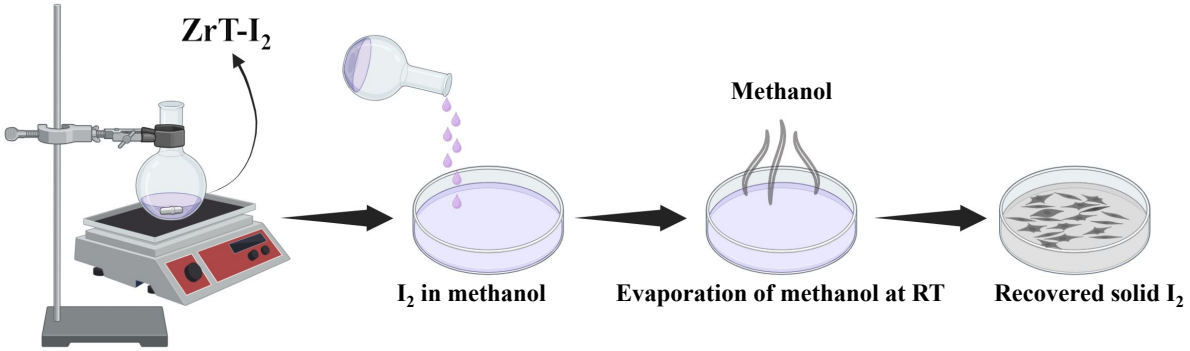

Figure S16. Schematic illustration for recovery of solid iodine crystals from ZrT-I_2 upon treatment with methanol

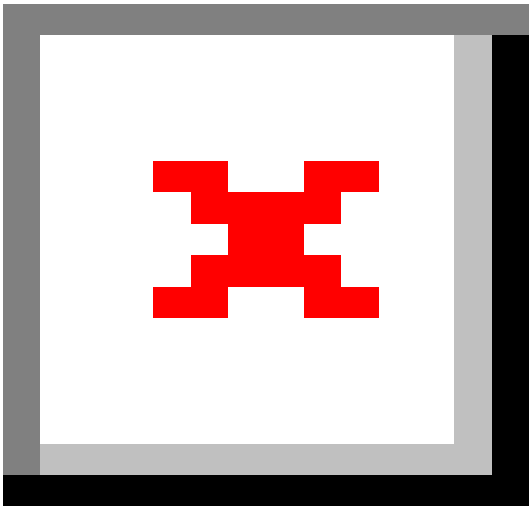

Figure S17. Digital images showing the recovery of solid iodine crystal by treatment of ZrT-I_2 with methanol

Table S7. Comparative analysis of iodine adsorption performance between ZrT and reported powder-form adsorbents

No.	Sorbent	Sorption Medium	Selectivity	Contact time	Max. Ads. Capacity (mg/g)	Ref.
1	MgAl-NO_3-LDH	Water	-	2 h	41.2	19
2	TAPB-BPDA COF	Water	-	90 min	988.17	20
3	Ag-NP zeolite	water	Cl^-, Br^-, CO_3^{2-}, CrO_4^{2-}	900 h	20.44	21
4	$Zn_9(btc)_4(atz)_{12}$	Cyclohexane	-	65 min	400	22
5	Th-BDAT	Cyclohexane	-	24 h	1046	23
6	PHCP	Water Cyclohexane	F^-, Cl^-, Br^-, CO_3^{2-}, NO_3^-, SO_4^{2-}	36 h	469.2 22.7	24
7	ECUT-Th-11	Cyclohexane	-	2 h	258.02	25
8	BDT-PT BDT-PA BDT-PB	Cyclohexane	-	72 h	504.4 664.6 537.4	26
9	Ni-MOF-74 Zr-UiO-66	Cyclohexane	Cl^-, CO_3^{2-}	48 h	680 170	27
10	n-CF@OCDs	Water	Cl^-, SO_4^{2-}, NO_3^-, Mg^{2+}, Na^+, Ca^{2+}	80 min	190.1	28
11	**ZrT**	**Vapor Water Cyclohexane**	**- Cl^-, Br^-, CO_3^{2-}, NO_3^-, SO_4^{2-}**	**90 h 90 min 150 min**	**1262.5 885.83 772.44**	**Present work**
12	NRPP-2	Cyclohexane	-	72 h	505.05	29
13	Zn(tr)(OAC) Zn(ttr)(OAC)	Water	Cl^-, CO_3^{2-}, NO_3^-, PO_4^{3-}	660 min	714.501 846.10	30
14	NiTi-S_x-LDH	Cyclohexane	-	55 h	527.4	31
15	iCON-4	Water	Cl^-, Br^-, NO_3^-, SO_4^{2-}	2 min	1632.1	32
16	$[Me_2NH_2][Sr_4(tatab)_3\text{-}(DMF)_{0.4}(H_2O)_{1.6}]$ $[Me_2NH_2]_5[La_3(\mu\text{-}O)(tatat)_2]$	Cyclohexane	-	72 h	168 226	33
17	HUN DHUN	Cyclohexane	-	72 h	90 130	34
18	Th-SINAP-7 Th-SINAP-8	Cyclohexane Vapor	- -	24 h 5 h	258 473	35
19	Al-APS Al-MAPS Al-DMAPS	Water	-	24 h	124 223 241	36
20	B-N@CS	Water	-	21 min	992.11	37
21	PTh PTh/α-MnO_2	Water	F^-, Cl^-, Br^-, NO_3^-, SO_4^{2-}, PO_4^{3-}	2 h	266.08 304.21	38
22	Ag/Cu-C	Water	Cl^-, CO_3^{2-}, SO_4^{2-}	-	247.1 (*p*H=3)	39

				510 min	116.1	
23	H_2CuY	Vapor	-	30 h	450	40
	COCuY				219	
24	PD-POP	Vapor	-		3530	41
	CD-POP			120 h	2600	
	BD-POP				840	

Table S8. Comparative analysis of iodine adsorption performance between ZrT@PVDF granules and reported non-powdered adsorbents

No.	Sorbent	Sorption Medium	Selectivity	Contact time	Max. Ads. Capacity (mg/g)	Ref.
1	δ-Bi2O3@PES granules	Water	Cl^-, CO_3^{2-}, NO_3^-, SO_4^{2-}	10 h	95.4	42
2	Alg-BO granules	Water	-	96 h	111.8	43
3	Bi2S3@PAN granules	Cyclohexane	-	14 h	943	44
4	**ZrT@PVDF granules**	**Vapor** **Water** **Cyclohexane**	**-** **Cl^-, Br^-, CO_3^{2-}, NO_3^-, SO_4^{2-}**	**90 h** **90 min** **150 min**	**945.2** **705.86** **598.38**	**Present work**
5	BN Foam	n-Hexane	-	18 h	61.33	45
6	PVDF/ZIF-8 Nanocomposite membrane	Water	-	33 h	73.33	46
7	Cross-linked chitosan microspheres	Water	Cl^-, Br^-, CO_3^{2-}	30 min	111.4	47
8	P-CDMs granules	Water	-	2 h	668	48
9	AgCl@CM	Water	Cl^-, CO_3^{2-}	20 min	193.5	49
10	Cu-BTC@PES	Vapor	-	~75 h	639	50

References:

1. P. H. M. Andrade, H. Ahouari, C. Volkringer, T. Loiseau, H. Vezin, M. Hureau and A. Moissette, *ACS Applied Materials & Interfaces*, 2023, **15**, 31032-31048.
2. S. M. Purushothaman, M. F. Tronco, M. Ponçot, C. C.S, N. Guigo, M. Malfois, N. Kalarikkal, S. Thomas, I. Royaud and D. Rouxel, *ACS Applied Polymer Materials*, 2024, **6**, 8291-8305.
3. R. Das, S. Giri, A. L. King Abia, B. Dhonge and A. Maity, *ACS Sustainable Chemistry & Engineering*, 2017, **5**, 2711-2724.
4. G. B. B. Varadwaj, O. A. Oyetade, S. Rana, B. S. Martincigh, S. B. Jonnalagadda and V. O. Nyamori, *ACS Applied Materials & Interfaces*, 2017, **9**, 17290-17305.
5. S. U. Jan, A. Ahmad, A. A. Khan, S. Melhi, I. Ahmad, G. Sun, C.-M. Chen and R. Ahmad, *Environmental Science and Pollution Research*, 2021, **28**, 10234-10247.
6. Q. Liu, L.-B. Zhong, Q.-B. Zhao, C. Frear and Y.-M. Zheng, *ACS Applied Materials & Interfaces*, 2015, **7**, 14573-14583.
7. A. D. Dwivedi, S. P. Dubey, K. Gopal and M. Sillanpää, *Desalination*, 2011, **267**, 25-33.
8. I. Ali, I. Burakova, E. Galunin, A. Burakov, E. Mkrtchyan, A. Melezhik, D. Kurnosov, A. Tkachev and V. Grachev, *ACS Omega*, 2019, **4**, 19293-19306.
9. Y. Wang, T. Nakano, X. Chen, Y.-L. Xu, Y.-J. He, Y.-X. Wu, J.-Q. Zhang, W. Tian, M.-H. Zhou and S.-X. Wang, *Journal of Hazardous Materials*, 2024, **466**, 133437.
10. K. H. Chu, J. Debord, M. Harel and J.-C. Bollinger, *Industrial & Engineering Chemistry Research*, 2022, **61**, 6781-6790.
11. E. S. Dragan, D. F. Apopei Loghin and A. I. Cocarta, *ACS Applied Materials & Interfaces*, 2014, **6**, 16577-16592.
12. J. Gong, T. Liu, X. Wang, X. Hu and L. Zhang, *Environmental Science & Technology*, 2011, **45**, 6181-6187.
13. X. Luo, X. Lei, N. Cai, X. Xie, Y. Xue and F. Yu, *ACS Sustainable Chemistry & Engineering*, 2016, **4**, 3960-3969.
14. N. Kumar, H. Mittal, S. M. Alhassan and S. S. Ray, *ACS Sustainable Chemistry & Engineering*, 2018, **6**, 17011-17025.
15. F. Zhao, E. Repo, M. Sillanpää, Y. Meng, D. Yin and W. Z. Tang, *Industrial & Engineering Chemistry Research*, 2015, **54**, 1271-1281.
16. A. M. Alswieleh, *ACS Applied Polymer Materials*, 2023, **5**, 1334-1343.
17. L.-T. He, L.-D. Zhao, W. Sun, J. Fang, X.-W. Liu, J.-J. Qi, Y. Qian and H. Li, *Langmuir*, 2023, **39**, 15319-15327.
18. M. Patel, H. Lanakapati and K. Maheria, *ACS Applied Engineering Materials*, 2024, **2**, 1542-1560.
19. L. Kentjono, J. C. Liu, W. C. Chang and C. Irawan, *Desalination*, 2010, **262**, 280-283.
20. R. Chen, T. Hu and Y. Li, *Reactive and Functional Polymers*, 2021, **159**, 104806.
21. Z. Tauanov and V. J. Inglezakis, *Science of The Total Environment*, 2019, **682**, 259-270.
22. Z.-Q. Jiang, F. Wang and J. Zhang, *Inorganic Chemistry*, 2016, **55**, 13035-13038.
23. Y. Ju, Z.-J. Li, J. Qiu, X. Li, J. Yang, Z.-H. Zhang, M.-Y. He, J.-Q. Wang and J. Lin, *Inorganic Chemistry*, 2023, **62**, 8158-8165.
24. J. Ma, Z. Shi, T. Wang, X. Huang, Y. Zhao, J. Wang, J. Li, D. Wang, L. Sun, G. Dong and M. Zhao, *ACS Sustainable Chemistry & Engineering*, 2024, **12**, 12113-12125.
25. L. Zhang, H. Lan, H. Wang, W. Zhang, F. Luo and L. Wang, *Inorganic Chemistry*, 2024, DOI: 10.1021/acs.inorgchem.4c02871.
26. Y. Ji, J. Huang, C. Liu, C. Ni, H. Yan, Y. David and Y. Qin, *ACS Applied Polymer Materials*, 2024, **6**, 7478-7487.
27. T. Alghamdi, P. O. Aina, A. A. Rownaghi and F. Rezaei, *ACS Applied Materials & Interfaces*, 2023, **15**, 33621-33632.
28. B. Zheng, X. Liu, J. Hu, F. Wang, X. Hu, Y. Zhu, X. Lv, J. Du and D. Xiao, *Journal of Hazardous Materials*, 2019, **368**, 81-89.
29. Y. H. Abdelmoaty, T.-D. Tessema, F. A. Choudhury, O. M. El-Kadri and H. M. El-Kaderi, *ACS Applied Materials & Interfaces*, 2018, **10**, 16049-16058.

30. J. Qin, W. Zhang, Y. Chen, R. Liu and Y. Fan, *Environmental Science and Pollution Research*, 2021, **28**, 28797-28807.
31. G. Lin, L. Zhu, T. Duan, L. Zhang, B. Liu and J. Lei, *Chemical Engineering Journal*, 2019, **378**, 122181.
32. Prince, A. Hassan, S. Chandra, A. Alam and N. Das, *RSC Sustainability*, 2023, **1**, 511-522.
33. X.-F. Zhong, Z.-C. Ma, J.-J. Lin, Y. Wu, G. Liang, Y.-Y. Zhang, D.-J. Chen, K.-P. Xie, Z.-W. Mo and X.-M. Chen, *Crystal Growth & Design*, 2023, **23**, 8793-8799.
34. Y. Guan, Y. Li, J. Zhou, T. Zhang, J. Ding, Z. Xie and L. Wang, *Inorganic Chemistry*, 2021, **60**, 9848-9856.
35. Z.-J. Li, Z. Yue, Y. Ju, X. Wu, Y. Ren, S. Wang, Y. Li, Z.-H. Zhang, X. Guo, J. Lin and J.-Q. Wang, *Inorganic Chemistry*, 2020, **59**, 4435-4442.
36. M. Alsalbokh, N. Fakeri, S. Lawson, A. A. Rownaghi and F. Rezaei, *Chemical Engineering Journal*, 2021, **415**, 128968.
37. M. A. Bhakare, K. D. Lokhande, P. S. Dhumal, M. P. Bondarde and S. Some, *Separation and Purification Technology*, 2021, **278**, 119490.
38. A. Waghmare, R. Rathore, A. Pandey and V. Chandra, *Colloids and Surfaces C: Environmental Aspects*, 2023, **1**, 100017.
39. C.-H. Gong, Z.-Y. Li, K.-W. Chen, A.-T. Gu, P. Wang and Y. Yang, *Journal of Environmental Radioactivity*, 2023, **265**, 107211.
40. J. Zhou, Q. Chen, T. Li, T. Lan, P. Bai, F. Liu, Z. Yuan, W. Zheng, W. Yan and T. Yan, *Inorganic Chemistry*, 2022, **61**, 7746-7753.
41. S. Bera, K. Garg and S. K. Samanta, *ACS Applied Nano Materials*, 2024, **7**, 1797-1803.
42. Q. Zhao, G. Chen, Z. Wang, M. Jiang, J. Lin, L. Zhang, L. Zhu and T. Duan, *Chemical Engineering Journal*, 2021, **426**, 131629.
43. T.-H. Kim, C. Seo, J. Seon, A. Battulga and Y. Hwang, 2022, **23**, 12225.
44. Q. Yu, X. Jiang, Z. Cheng, Y. Liao, Q. Pu and M. Duan, *New Journal of Chemistry*, 2020, **44**, 16759-16768.
45. G. Li, Y. Huang, J. Lin, C. Yu, Z. Liu, Y. Fang, Y. Xue and C. Tang, *Chemical Engineering Journal*, 2020, **382**, 122833.
46. X. Long, Y.-S. Chen, Q. Zheng, X.-X. Xie, H. Tang, L.-P. Jiang, J.-T. Jiang and J.-H. Qiu, *Separation and Purification Technology*, 2020, **238**, 116488.
47. W. Zhang, Q. Li, Q. Mao and G. He, *Carbohydrate Polymers*, 2019, **209**, 215-222.
48. J.-X. Wang, H.-R. Shu, K. Guo, X. Wang and S. Zhang, *Journal of Materials Science*, 2024, **59**, 3327-3338.
49. Q. Li, Q. Mao, M. Li, S. Zhang, G. He and W. Zhang, *Carbohydrate Polymers*, 2020, **234**, 115926.
50. Q. Zhao, L. Zhu, G. Lin, G. Chen, B. Liu, L. Zhang, T. Duan and J. Lei, *ACS Applied Materials & Interfaces*, 2019, **11**, 42635-42645.